IOP Publishing Measurement Science and Technology
Meas. Sci. Technol. 31 (2020) 045004 (10pp) https://doi.org/10.1088/1361-6501/ab4eb8

Independent temporal and spatial variation analysis of ionospheric TEC over Asia-Pacific area based on BDS GEO satellites

Xiaotao Bai and Changsheng Cai[1]

School of Geosciences and Info-Physics, Central South University, Changsha 410083, People's Republic of China

E-mail: cscai@hotmail.com and x_t_bai@163.com

Received 26 June 2019, revised 11 October 2019
Accepted for publication 17 October 2019
Published 6 January 2020

Abstract

GPS has been widely used to monitor ionospheric total electron content (TEC) variations. However, GPS-derived TEC contains ionospheric horizontal gradient information due to the motion of GPS satellites. As a result, the temporal and spatial variation information is mixed. With the advent of the geostationary earth orbit (GEO) of the BeiDou navigation satellite system (BDS), observations from BDS GEO satellites provide a new opportunity for independent research on the temporal and spatial variations of the ionospheric TEC. Furthermore, the GEO satellite also enables continuous and long-term TEC monitoring. Due to its higher orbit, the BDS GEO-derived TEC also contains more plasmaspheric electron content. In this study, the temporal and spatial variation characteristics of the ionospheric TEC derived from the BDS GEO satellites over the Asia-Pacific area are investigated. The achievable TEC theoretical accuracy from the BDS GEO measurements is first deduced. The TEC time series at 26 BDS stations over the Asia-Pacific area is then analyzed. Results acquired from the vertical TEC (VTEC) observations in 2017 indicate obvious periodic variations and spatial variations with a semi-annual anomaly. Through an analysis of the VTEC series over a span of five years, it is revealed that the long-term TEC variations are quite dependent on the solar activity intensity in terms of the F10.7 index. Besides, the BDS GEO-derived VTEC variation trend is consistent with those acquired from the global ionospheric map (GIM) and the NeQuick model. However, significant biases exist at some stations due to uneven accuracy of the two global ionospheric models. The maximum RMS discrepancies reach 4.3 TECU and 9.9 TECU for the GIM and NeQuick, respectively.

Keywords: BeiDou navigation satellite system, geostationary earth orbit, total electron content, temporal variation, spatial variation

(Some figures may appear in colour only in the online journal)

1. Introduction

The ionosphere plays an important role in fields where trans-ionospheric electromagnetic wave signals are used such as satellite navigation, radio communication and radar detection. Understanding the ionospheric temporal and spatial variation characteristics is vital for precisely modeling and forecasting of the ionosphere. As the ionosphere is a dispersive media, the global navigation satellite system (GNSS) signal refraction depends on its frequency. Utilizing this property, the GPS dual-frequency signal has been broadly applied to monitor the ionospheric total electron content (TEC) due to its advantages of high accuracy, low cost, all weather and all time. However, the GPS-derived TEC contains ionospheric horizontal gradient information due to the moving ionospheric pierce points (IPPs) caused by the motion of GPS satellites. As a result,

[1] Author to whom any correspondence should be addressed.

the acquired TEC time series comprises mixed temporal and spatial variation information. With the advent of the quasi-invariant geostationary earth orbit (GEO) of the BeiDou navigation satellite system (BDS), measurements from the BDS GEO satellites offer a condition to investigate the temporal and spatial variations of the ionospheric TEC separately. Furthermore, the geostationary orbit also enables continuous and long-term TEC monitoring with even a single GEO satellite, facilitating the analysis and understanding of its detailed variation characteristics. Besides, the BDS GEO-derived TEC also contains more plasmaspheric electron content due to its higher orbital altitude.

In recent decades, the GNSS technique has been widely used as an important means to investigate ionospheric TEC variations [1–6]. The temporal variations of the ionospheric TEC exhibit different scales. Liu analyzed the 11-year TEC data acquired from the Jet Propulsion Laboratory (JPL) global ionospheric map (GIM) from 1998 to 2008 and found that the TEC data had strong solar cycle, annual/semi-annual and 27 d variations [7]. Wu investigated both the temporal and spatial variations of the ionospheric TEC in Victoria using GPS dual-frequency data over a period of two years and stated that it was challenging to precisely represent the behavior of the ionosphere due to its complexity [8]. Tariku analyzed the diurnal, monthly and seasonal variations of the GPS-derived vertical TEC (VTEC) over low-latitude regions during low and high solar activity phases [9]. Şentürk and Çepni analyzed the diurnal, monthly, seasonal and annual variations of VTEC values derived from the Center for Orbit Determination in Europe (CODE) GIM data [3]. GNSS network measurements are a powerful tool for studying the global pattern and evolution process of the ionospheric TEC variations [1]. By detecting and analyzing ionospheric responses, the GPS observations can be used for investigating various natural phenomena such as earthquakes, geomagnetic storms, solar eclipses and solar flares [10–14].

The existing research work is mostly based on the GPS. With the rapid development of the BDS, five BDS GEO satellites have been operational in orbit so far. The unique feature of the BDS GEO satellites attracts increasing attention in ionospheric study. Yang compared the precision of the VTEC derived from the BDS GEO B_1/B_2, B_1/B_3 and B_2/B_3 dual-frequency observations and results indicated that the phase-smoothed B_1/B_2 code observations achieved the highest precision [15]. Jin pointed out that the BDS GEO observations became an important data source to observe ionospheric responses to geomagnetic storms [16]. In summary, the availability of the BDS GEO observations provides a new means for monitoring the ionospheric TEC. In this study, the BDS GEO satellites are utilized to independently investigate temporal and spatial variation characteristics of the ionospheric TEC over the Asia-Pacific area by taking advantage of the unique features of the GEO satellites. The observations collected from all available BDS GEO satellites at 26 stations spanning five years are used for this study. In view of the higher accuracy of the real measured TEC from the BDS GEO satellites, the BDS GEO-derived TEC is also applied to assess the GIM and NeQuick models.

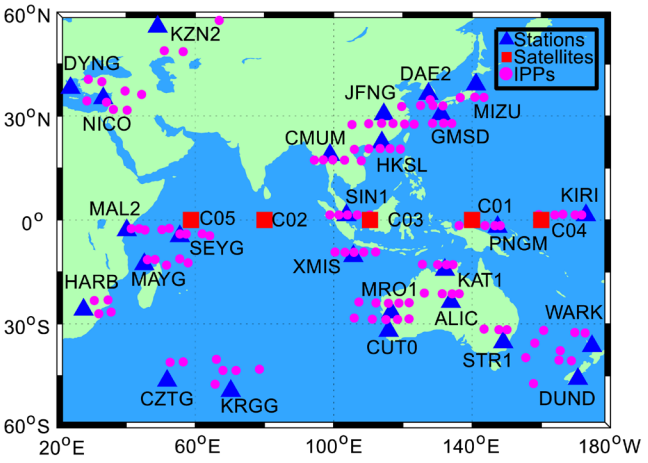

Figure 1. Station distribution, ground track of BDS GEO satellites and location of IPPs over the Asia-Pacific area.

2. Absolute ionospheric TEC retrieval from BDS GEO observations

Generally, dual-frequency code observations can be used to calculate the ionospheric TEC. In view of the larger noise level of code observations, the carrier phase smoothed code observations are used to obtain the TEC, as follows [17]:

$$\mathrm{STEC} = \frac{f_1^2 f_2^2}{40.28 \times (f_1^2 - f_2^2)} \times (\phi_1^i \cdot \lambda_1 - \phi_2^i \cdot \lambda_2 + \bar{N}_\mathrm{m} + b^\mathrm{s} + b_\mathrm{r}), \tag{1}$$

$$\bar{N}_\mathrm{m} = \frac{1}{m} \sum_{k=1}^{m} (P_2^i - P_1^i - (\phi_1^i \cdot \lambda_1 - \phi_2^i \cdot \lambda_2)), \tag{2}$$

where STEC is the slant TEC along the satellite-receiver line of sight, φ_1 and φ_2 represent the measured carrier phase on B_1 and B_2 frequency bands of BDS GEO satellites, respectively, i represents a BDS GEO satellite, f_1 and f_2 are the carrier phase frequencies, λ_1 and λ_2 are the carrier phase wavelengths on B_1 and B_2, respectively, b^s and b_r represent the differential code bias (DCB) at satellite and receiver ends, respectively, $\bar{N}_\mathrm{m}$ is a linear combination of carrier phase and code observations, which can be depicted by (2), P_1 and P_2 represent code observations on B_1 and B_2, respectively and m is the number of epochs for smoothing code observations. Prior to computing the TEC, cycle slips were detected and corrected by jointly using a forward and backward moving window averaging algorithm and a second-order, time-difference phase ionospheric residual algorithm [18]. In order to acquire the absolute ionospheric TEC, it is necessary to make the DCB corrections to remove the b^s and b_r [17]. The DCB correction data is available from the International GNSS Service (IGS).

In (1), the precision of the STEC is dominated by the precisions of determining the $\bar{N}_\mathrm{m}$, b^s and b_r, since the carrier phase observation has a noise level of one or two millimeters [19].

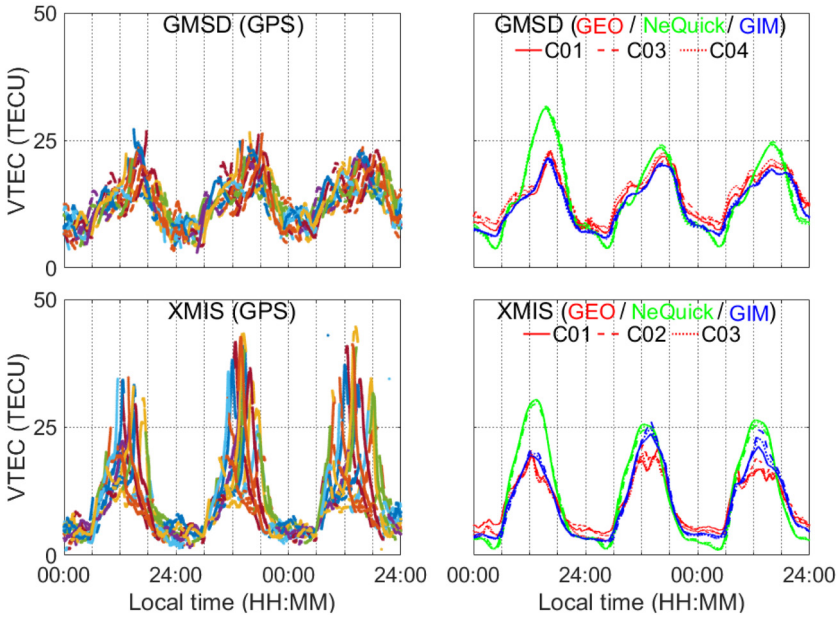

Figure 2. Diurnal ionospheric VTEC variations derived from different data sources on the three consecutive days from 31 May to 2 June 2017.

Following the error propagation law, the standard deviation of the STEC can be expressed below after neglecting the errors of the carrier phase observations and assuming no correlation among the $\bar{N}_{\mathrm{m}}$, b^{s} and b_{r}.

$$\delta_{\mathrm{STEC}} = \frac{f_1^2 f_2^2}{40.28 \times (f_1^2 - f_2^2)} \sqrt{\delta_{\bar{N}_{\mathrm{m}}}^2 + \delta_{b^{\mathrm{s}}}^2 + \delta_{b_{\mathrm{r}}}^2}, \tag{3}$$

where $\delta_{\bar{N}_{\mathrm{m}}}$, $\delta_{b^{\mathrm{s}}}$ and $\delta_{b_{\mathrm{r}}}$ are the standard deviations of the $\bar{N}_{\mathrm{m}}$, b^{s} and b_{r}, respectively. For BDS GEO satellites, $f_1 = 1561.098$ MHZ and $f_2 = 1207.14$ MHZ, equation (3) can be rewritten as,

$$\delta_{\mathrm{STEC}} = 8.998 \sqrt{\delta_{\bar{N}_{\mathrm{m}}}^2 + \delta_{b^{\mathrm{s}}}^2 + \delta_{b_{\mathrm{r}}}^2}. \tag{4}$$

Following the error propagation law, the standard deviation of the $\bar{N}_{\mathrm{m}}$ in (2) can be expressed below after assuming that the code observations on B_1 and B_2 have an equal noise level of δ_{P} in unit of meters,

$$\delta_{\bar{N}_{\mathrm{m}}} = \sqrt{\frac{2}{m}} \delta_{\mathrm{P}}^2. \tag{5}$$

Substituting $\delta_{\bar{N}_{\mathrm{m}}}$ into (4), the following (6) can be obtained as,

$$\delta_{\mathrm{STEC}} = 8.998 \sqrt{\frac{2}{m} \delta_{\mathrm{P}}^2 + \delta_{b^{\mathrm{s}}}^2 + \delta_{b_{\mathrm{r}}}^2}. \tag{6}$$

The DCB products provided by the IGS have an accuracy of better than 0.5 ns [20–22]. The noise of the BDS GEO code observations is typically at a level of 0.2 m [19]. Suppose that the carrier phase observations of at least 12 epochs are used for smoothing the code observations, the δ_{STEC} can achieve an accuracy of 2 TECU according to (6). Such accuracy is comparable to that derived from the absolute GPS TEC [23].

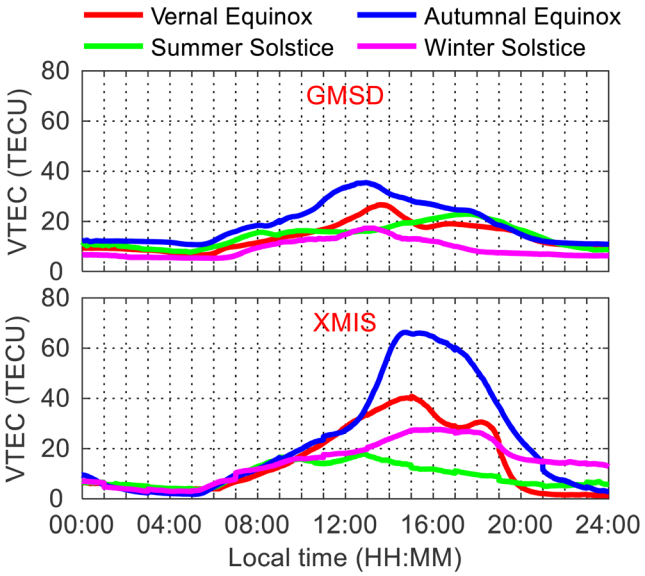

Figure 3. Ionospheric VTEC variations at GMSD and XMIS on four days of different seasons in 2017.

The STEC can be further converted into VTEC via a projection using the following mapping function [24]:

$$F(Z) = \left\{ 1 - \left[\frac{R_{\mathrm{E}} \sin(Z)}{R_{\mathrm{E}} + H_{\mathrm{ion}}} \right]^2 \right\}^{-0.5}, \tag{7}$$

where $F(Z)$ is the projection function, R_{E} is the Earth's radius, the ionosphere is hypothetically condensed into a thin shell at an altitude of 300–450 km [25], H_{ion} is the altitude of the ionospheric thin shell and Z is the zenith distance of the satellite relative to the receiver.

3. Data description

In order to analyze the temporal and spatial variation characteristics of the ionospheric TEC, BDS GEO data sets collected at a total of 26 multi-GNSS experiment (MGEX) stations over the Asia-Pacific area are used. These stations are distributed in a latitude range from 60° S–60° N and a longitude range from 20° E–180° E. In such an area, more BDS GEO satellites can be observed, since their orbits are located vertically above the equator. The station distribution, ground track of BDS GEO satellites and locations of IPPs are shown by triangle, square and circle markers with different colors in figure 1, respectively. The observations have a sampling interval of 30 s. The satellite mask elevation angle is set to 10°. Daily BDS DCB products for both the satellite and receiver provided by the CODE are used for DCB corrections to obtain absolute TEC values.

In addition to the BDS GEO satellites, the ionospheric TEC can still be obtained via the GIM and NeQuick. The CODE-generated GIM products are derived based on a spherical harmonic assumption of the ionosphere at a thin-shell height [26]. The GIM contains VTEC in a globally-distributed grid, covering a latitude range from +87.5° to −87.5° with a resolution of 2.5° and a longitude range from −180° to +180° with a resolution of 5°. The TEC map is updated at an interval of one or two hours. The NeQuick is a 3D and time-dependent ionospheric electron density model, which can be used to calculate the electron concentration at any given location in the ionosphere. Thus, the TEC at a global scale may be derived by means of numerical integration along the receiver-to-satellite ray path. The NeQuick model has been adopted by the Galileo system for ionospheric delay corrections [27].

4. Temporal variation of ionospheric TEC

4.1. Diurnal variation of ionospheric VTEC

Due to their quasi-invariant geostationary orbits, the BDS GEO satellites can be used to consecutively monitor the ionospheric TEC variations at almost the same spatial location. Figure 2 shows diurnal ionospheric VTEC variations on three consecutive days of 31 May–2 June 2017 at the GMSD and XMIS stations using the BDS GEO satellites as well as the GPS satellites, GIM and NeQuick for comparison. The GSMD and XMIS stations are located in the middle-latitude area of the northern hemisphere and the low-latitude area of the southern hemisphere, respectively. Observations from the GEO satellites C01, C03 and C04 at GMSD and C01, C02 and C03 at XMIS are available during the three consecutive days. At both stations, the satellite elevation angles of these GEO satellites are over 40°. The left panels show the VTEC time series derived from all observed GPS satellites whereas the right panels show the VTEC acquired from the three BDS GEO satellites as well as the GIM and NeQuick. In the left panels, different colors of curves represent the TEC time series measured from different GPS satellites. It is explicit that multiple GPS satellites are required to depict a complete diurnal variation of the ionospheric VTEC, since a single GPS satellite is only visible over a few hours. Furthermore, the depicted diurnal variations are coarse due to an effect of the simultaneous spatial variations. By contrast, the BDS GEO-derived VTEC time series is continuous, as can be seen from the red curves in the right panels, since the GEO satellites are almost stationary, which enables the VTEC diurnal variation to be depicted with even one GEO satellite. Besides, the TEC derived from the BDS GEO satellites contains electronic content up to a height of 36 000 km whereas the TEC derived from the GPS contains electronic content up to the height of 20 200 km. As a result, the BDS GEO-derived TEC includes more contribution from the plasmasphere.

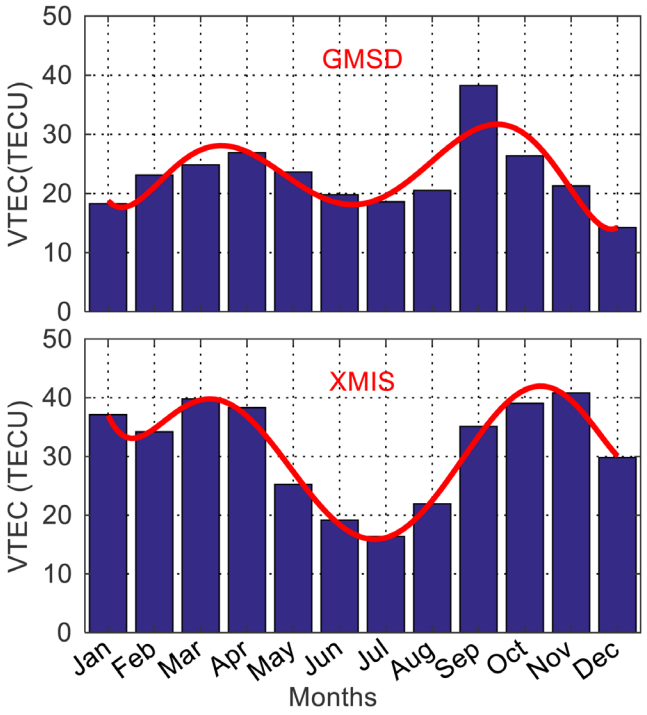

Figure 4. Monthly average ionospheric VTEC at GMSD and XMIS in 12 months of 2017.

The blue and green curves represent the GIM- and NeQuick-derived VTEC time series at the IPPs, respectively. It is obvious that the GIM and NeQuick models cannot exhibit detailed variation of the VTEC well when compared with the real measured VTEC from the BDS GEO satellites. The NeQuick-derived VTEC obviously deviates the measured VTEC from the BDS GEO satellites, since the NeQuick is only a semi-empirical model. At XMIS, a maximum discrepancy reaches 15 TECU at 14:00 on 31 May 2017. By contrast, the GIM-derived VTEC values are closer to those acquired from the BDS GEO satellites since the GIM is generated on the basis of measured TEC. In summary, all these data sources exhibit a consistent diurnal variation trend of the ionospheric VTEC.

4.2. Seasonal variation of ionospheric VTEC

Ionospheric TEC has been well known to exhibit seasonal variation behavior [7]. Generally, a year may be divided into four seasons. They are spring (March, April and May), summer

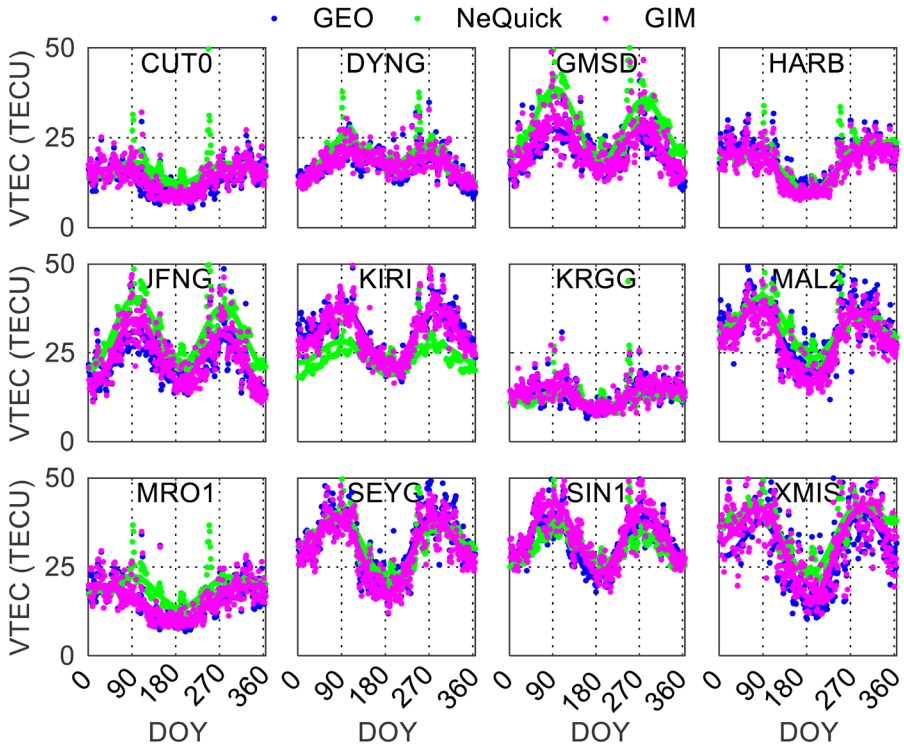

Figure 5. Daily ionospheric VTEC variations in the entire year of 2017 at 12 stations. The12 stations are distributed in different latitudes.

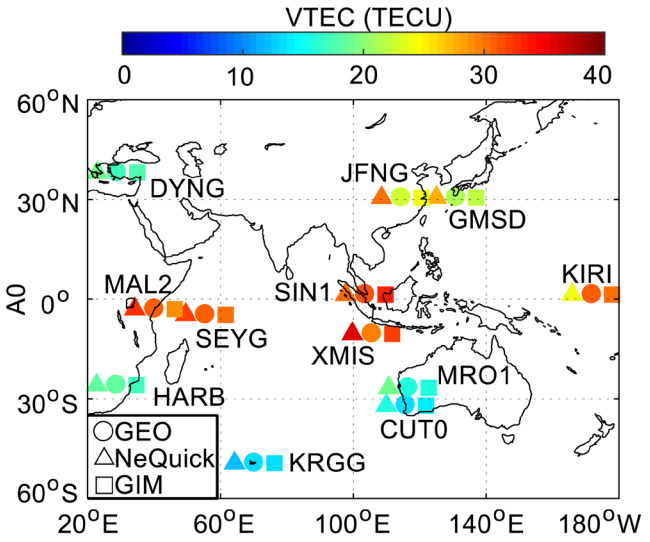

Figure 6. Geographical distribution of yearly average VTEC (A_0) at different stations at daytime in 2017.

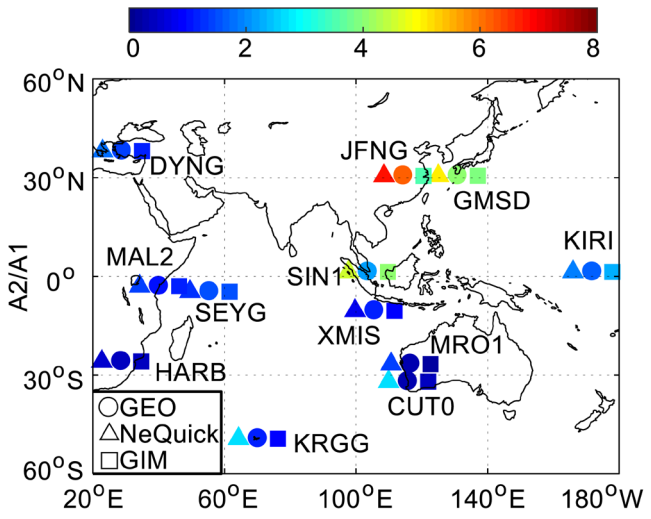

Figure 7. Geographical distribution of relative magnitudes (A_2/A_1) at different stations at daytime in 2017.

(June, July and August), autumn (September, October and November) and winter (December, January and February) in the northern hemisphere [8]. In the southern hemisphere, the seasons have perfect symmetry. To understand seasonal variation characteristics, figure 3 shows the diurnal variations of the ionospheric VTEC derived from the BDS GEO satellites of C01 at the northern hemisphere GMSD station and C03 at the south-hemisphere XMIS station on four days of different seasons in 2017, namely the vernal equinox, summer solstice, autumnal equinox and winter solstice. The two satellites are chosen due to their highest elevations among all visible BDS GEO satellites. As observations are incomplete at GMSD on the exact days of the vernal equinox, summer solstice and autumnal equinox, data sets on adjacent days i.e. March 21, June 23 and October 01 are used as a substitute. The ionospheric VTEC curves on the four different days are plotted with different colors to reflect the diurnal variations in the four different seasons. It can be seen that the VTEC curves have larger variation amplitudes at XMIS due to its lower latitude in comparison to the GMSD station. At both stations, the daily VTEC peak values on the vernal equinox or autumnal equinox are larger than those on the summer solstice or winter solstice, indicating an obvious seasonal variation. Figure 3 also shows that the ionospheric VTEC values at GMSD are higher on the summer solstice than those on the winter solstice, but it is the

Table 1. Annual variation phase D_1 and semi-annual variation phase D_2 at different stations (DOY).

	CUT0	DYNG	GMSD	HARB	JFNG	KIRI	KRGG	MAL2	MRO1	SEYG	SIN1	XMIS
D1	1	166	165	363	142	2	359	7	365	363	8	361
D2	110	94	91	92	95	99	98	90	93	90	90	100

opposite at XMIS. This is because the two stations are located in two different hemispheres and the seasons are the opposite in the two hemispheres.

To further analyze the seasonal variations, figure 4 shows the monthly average ionospheric VTEC at GMSD and XMIS in the entire year of 2017. The statistics are based on the VTEC values at the local time (LT) of 14:00 of each day. In order to clearly depict the seasonal variation, six-order polynomial fitting curves are displayed with orange colors. It is explicit that the ionospheric VTEC at both stations exhibits an obvious seasonal variation. At GMSD, the maximum value of the ionospheric VTEC appears at 38 TECU in September whereas the minimum value appears at 14 TECU in December. A similar phenomenon occurs at XMIS where the maximum monthly average VTEC value appears at 40 TECU in November whereas the minimum VTEC takes place at 16 TECU in July. At both stations, the peak of the VTEC variations emerges in spring/autumn whereas the trough of the VTEC variations takes place in summer/winter, which indicates an occurrence of a semi-annual anomaly phenomenon [28]. The ionospheric TEC in the summer is higher than that in the winter at both stations, and no winter anomaly phenomenon is found.

4.3. Semi-annual and annual variations of ionospheric VTEC

To analyze semi-annual and annual variations of the ionospheric TEC, the daily VTEC time series can be mathematically expressed in three terms, namely the average, annual and semi-annual components, based on the Fourier analysis method as follows [29]:

$$\mathrm{VTEC}(d,t) = A_0(t) + A_1(t)\cos\frac{2\pi}{T}[d - D_1(t)] + A_2(t)\cos\frac{4\pi}{T}[d - D_2(t)], \quad (8)$$

where d is day of year (DOY) and T ($T = 365.25$) is number of days in a year, t is LT, A_0 is yearly average value of VTEC time series, A_1 and A_2 are amplitudes of the VTEC annual and semi-annual components, respectively, and D_1 and D_2 are the corresponding phases, denoting the days when the maximal VTEC values appear. By comparing coefficients A_1 and A_2 with A_0, the annual and semi-annual variation intensities can be acquired.

The BDS GEO data sets at 12 stations with different latitudes are used to analyze the annual and semi-annual variations of the VTEC. Figure 5 shows the daily ionospheric VTEC variations at daytime in the entire year of 2017. The VTEC value at LT 14:00 is used to represent the daily VTEC at each station. The VTEC time series derived from the GIM and NeQuick at the IPPs at the same moment is also displayed for comparison . The blue, green and pink dots represent the daily

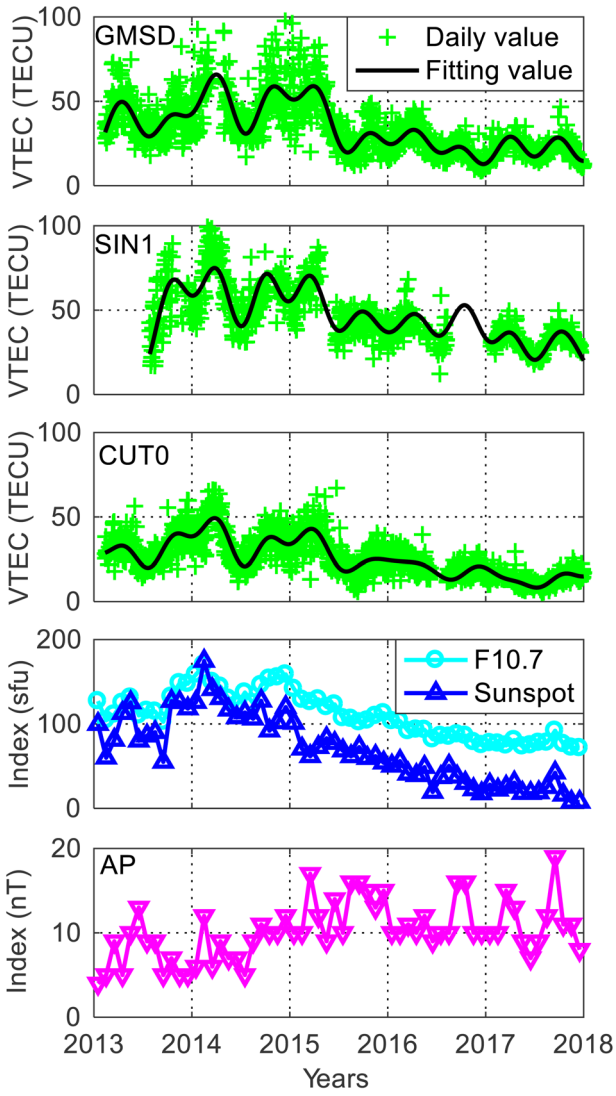

Figure 8. Long-term variations of ionospheric VTEC based on BDS GEO satellites.

VTEC from the BDS GEO, NeQuick and GIM, respectively. In order to reflect the variation trend, the corresponding fitting curves based on the equation (8) are also displayed. As can be seen from the fitting curves, the peaks appear twice, indicating apparent semi-annual variations. The two peak days are close to vernal equinox and autumnal equinox, respectively.

The GEO-, GIM- and NeQuick-derived VTEC time series have a consistent varying trend. However, the green curves significantly deviate from the blue curves at some stations such as GMSD, JFNG, KIRI, MAL2, MRO1 and XMIS, indicating that the NeQuick-derived VTEC values have relatively larger errors in the low-latitude area. Using the real measured VTEC from the BDS GEO satellites as references, the station-averaged RMS discrepancies for the NeQuick- and

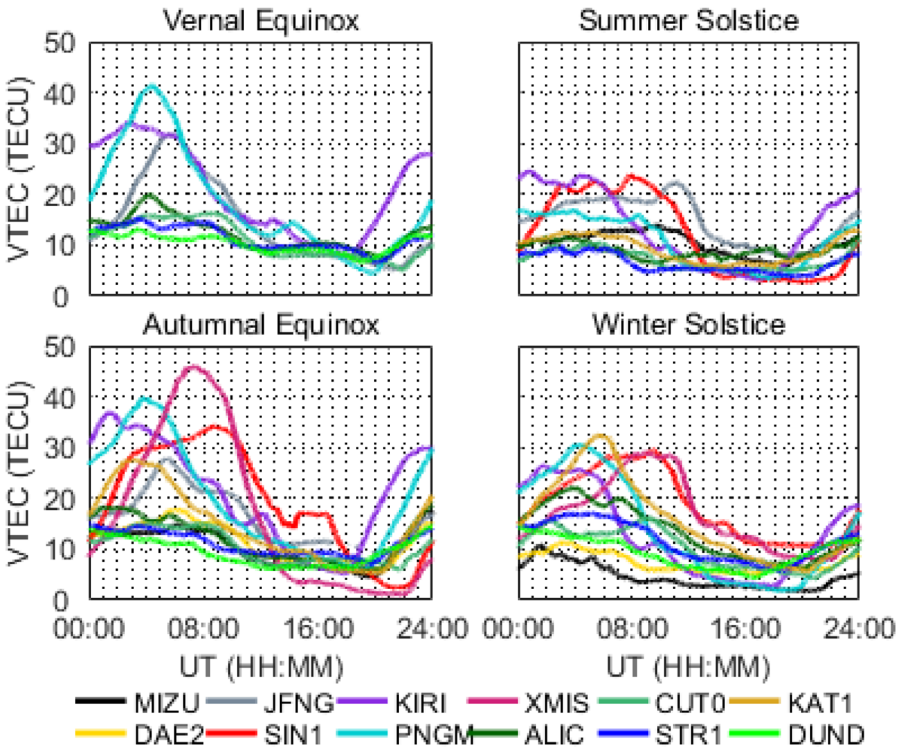

Figure 9. Diurnal variations of ionospheric VTEC derived from BDS GEO satellite C01 at 12 stations on four days of different seasons, namely the vernal equinox, summer solstice, autumn equinox and winter solstice in 2017.

GIM-derived VTEC are 6.2 TECU and 2.5 TECU, respectively. The maximum RMS for the NeQuick-derived VTEC reaches 9.9 TECU at XMIS. By contrast, the GIM-derived VTEC values are closer to the reference values. The maximum RMS is 4.3 TECU at SIN1. According to previous analysis, the GEO-derived TEC has an accuracy of 2 TECU. The larger discrepancies at some stations indicate a nonuniform accuracy of the NeQuick and GIM in the Asia-Pacific area.

To further investigate the annual and semi-annual variations of the ionospheric VTEC over the Asia-Pacific area, the Fourier analysis method, as shown in (8), is applied and then the coefficients of A_0, A_1 and A_2 can be obtained. The A_0 is the yearly average value of the VTEC, while the A_1 and A_2 denote the amplitudes of the annual and semi-annual components, respectively. Figure 6 shows the yearly average value of the VTEC at different stations at daytime in 2017. The circle marker at the station location represents the A_0 acquired from the BDS GEO observations whereas the adjacent triangle and square markers indicate the A_0 derived from the NeQuick and GIM, respectively. The A_0 remains within 40 TECU. In addition, the A_0 is significantly larger in the low-latitude area than those in the middle and high-latitude areas. On the whole, the yearly average value of the VTEC derived from the GEO satellites, NeQuick and GIM agree well. The yearly average values of the NeQuick-derived VTEC differ obviously, at the JFNG, GMSD, XMIS and KIRI stations, from the GEO-derived VTEC, suggesting larger errors of the NeQuick-derived VTEC at these stations. The maximum difference of the yearly average values reaches 7.1 TECU at JFNG. By contrast, the yearly average values from the GIM-derived VTEC are closer to those acquired from the GEO-derived VTEC. Their maximum difference is 2.7 TECU at XMIS.

Figure 7 shows the geographical distribution of the relative magnitudes of A_2/A_1 at different stations at daytime in 2017. The ratios are larger than 1 at most stations, which indicates that the semi-annual variation of the ionospheric VTEC over the Asia-Pacific area in 2017 is dominant, as opposed to the annual variation. The semi-annual variation amplitudes are much larger than their annual variation amplitudes at JFNG and GMSD in the northern hemisphere, since their ratios of A_2/A_1 reach 4. But at the stations of HARB, MRO1 and CUT0 in the southern hemisphere, the ratios of A_2/A_1 are lower than 0.5, indicating a dominant annual variation at the three stations.

Table 1 shows the annual variation phase D_1 and semi-annual variation phase D_2 at different stations. The phase represents the day of the year when the VTEC reaches its maximal value. It is found that D_1 is close to the summer solstice at the northern hemisphere stations of DYNG, GMSD and JFNG whereas D_1 is close to the winter solstice at the other stations located in the southern hemisphere or near the equator, which suggests that the maximum VTEC value in the annual variation appears in the local summer season after taking the season symmetry into account. Differing from the annual variation, the semi-annual variation phase appears in the local spring or autumn seasons, indicating an occurrence of the semi-annual anomaly. This confirms once again the existence of the semi-annual anomaly phenomenon.

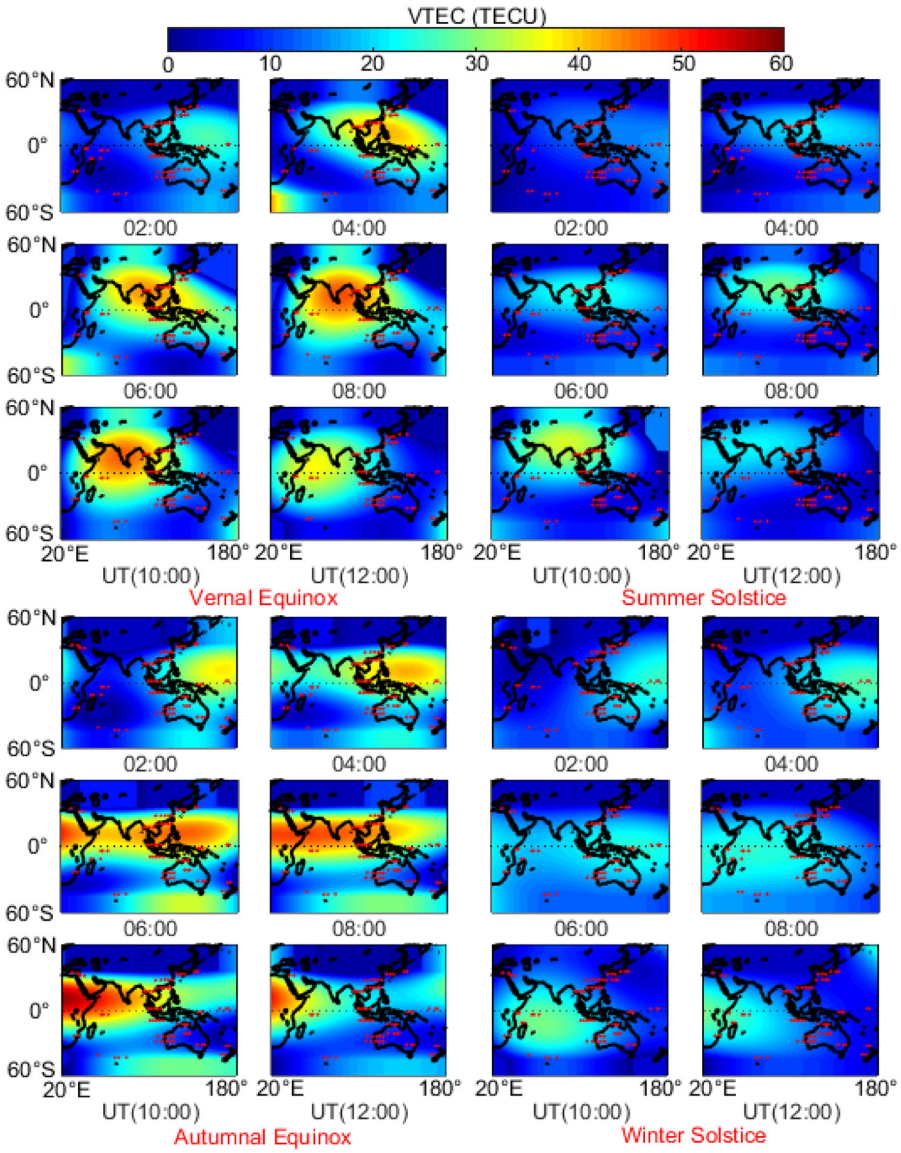

Figure 10. Spatial distribution of ionospheric VTEC derived from BDS GEO satellites over the Asia-Pacific area on four days of different seasons.

4.4. Long-term variation of ionospheric VTEC

To analyze long-term variations of the ionospheric VTEC, the VTEC time series is derived from the BDS GEO satellites of C01 at GMSD, C03 at SIN1 and CUT0 over a span of five years from 2013–2017. Again, the VTEC value at LT 14:00 of each day is used to represent the daily VTEC. The three stations are located close to the north latitude of 30°, the equator and south latitude of 30°, respectively. Figure 8 shows the daily ionospheric VTEC time series with green plus markers. The discontinuity of the VTEC time series at all three stations is caused by the lack of observations. The daily VTEC values are fitted with six-term sine functions to indicate their variation trends, as can be seen from the black curves. It is noted that the VTEC time series has a large varying amplitude at all three stations before June 2015. Afterwards, the VTEC series fluctuates moderately. The stations of GMSD in the northern latitude and SIN1 near the equator exhibit larger VTEC values than the station of CUT0 in the southern latitude. In order to gain insight into the reasons for the long-term variations, the solar activity index F10.7, sunspot number and geomagnetic index are provided in the middle and bottom panels to indicate the solar activity intensity and the level of geomagnetic activity. The long-term VTEC variation has a strong correlation to the solar activity intensity in terms of the indices of F10.7. Their correlation coefficient reaches 0.7 at GMSD, 0.3 at SIN1 and 0.6 at CUT0. The relatively weaker correlation at SIN1 reflects that the ionosphere is more complex near the equator. By contrast, the long-term VTEC variation is less correlated to the geomagnetic index AP since their correlation coefficient is smaller than 0.1 at all three stations. In summary, the long-term VTEC variation is mainly dependent on solar activity intensity.

5. Spatial variation of ionospheric VTEC

Generally, the ionospheric VTEC varies with different spatial locations. In order to investigate spatial variation

characteristics of the ionospheric VTEC over the Asia-Pacific area, figure 9 shows the diurnal variations of the ionospheric VTEC derived from the same GEO satellite at different stations on four days of different seasons in 2017, namely vernal equinox, summer solstice, autumnal equinox and winter solstice. Data sets collected at twelve stations with different latitudes are used for this spatial variation analysis. These stations are located in both southern and northern hemispheres with a latitude span of around 84°. The GEO satellite C01 is commonly visible at these stations owing to its relatively higher satellite elevation angles. The VTEC curve at each station is plotted with a different color. Due to the lack of data at some stations, the number of the actually plotted VTEC curves is less than twelve on all four days, except for autumnal equinox. The maximum VTEC difference at the same moment among different stations is close to 20 TECU on the summer solstice and winter solstice and over 30 TECU on the vernal equinox and autumnal equinox. This phenomenon is caused by the solar intensity differences at different latitudes and LTs. The diurnal variations of the VTEC are obvious in most stations. However, the peaks of the VTEC curves appear at a different time for different stations. The peak times differ by several hours since the LTs are different for stations with different longitudes. Generally, the intensity of incident solar ray reaches its maximum value at noon of LTs. As a result, the diurnal VTEC peaks in this period.

Figure 10 shows the spatial distribution of the ionospheric VTEC derived from the BDS GEO satellites over the Asia-Pacific area by interpolating the VTEC at all 26 stations with a three-order polynomial fitting approach. The diurnal VTEC variations are displayed every two hours from universal time (UT) 2:00–12:00 on four different days of the vernal equinox, summer solstice, autumn equinox and winter solstice. The red dots represent the locations of the IPPs. As can be seen from these panels at an interval of two hours, the diurnal VTEC variations are obvious and the larger VTEC appears during the period of 4:00–10:00 of the center area. The VTEC variations at the low-latitude area are more active than the other areas. The maximum VTEC up to 50–60 TECU appears on the vernal equinox and autumn equinox. By contrast, the maximum VTEC values are slightly lower at around 35 TECU on the summer solstice and winter solstice. The maximum spatial difference at the same moment reaches 51 TECU, 39 TECU, 59 TECU and 30 TECU on the vernal equinox, summer solstice, autumn equinox and winter solstice, respectively. This reveals significant spatial difference over the Asia-Pacific area.

6. Conclusions

BDS GEO satellites can be tracked to monitor ionospheric TEC continuously. By taking advantage of their almost stationary satellite orbits, this study separately investigates the temporal and spatial variation characteristics of the ionospheric VTEC over the Asia-Pacific area based on the BDS GEO satellites. Following the error propagation law, the absolute TEC derived from the BDS GEO satellites has an accuracy of 2 TECU. By analyzing the BDS GEO-derived VTEC time series over the Asia-Pacific area in 2017, obvious diurnal, seasonal and semi-annual variations are found. According to the analysis of the monthly average ionospheric VTEC, it is revealed that the peak value of the VTEC variations emerges in spring/autumn whereas the trough of the VTEC variations takes place in summer/winter, indicating an occurrence of a semi-annual anomaly phenomenon. Based on the Fourier analysis results, it is found that the semi-annual variations of the ionospheric VTEC are dominant at most stations. The BDS GEO-derived VTEC variation trend is consistent with those acquired from the GIM and NeQuick model. However, significant biases exist at some stations. The maximum RMS discrepancies for the GIM- and NeQuick-derived VTEC reach 4.3 TECU and 9.9 TECU, respectively, indicating an uneven accuracy distribution of the two global ionospheric models. Based on the analysis using data sets spanning from 2013–2017, the long-term VTEC variations are quite dependent on solar activity intensity in terms of the index of F10.7 with a maximal correlation coefficient of 0.7.

The BDS GEO data sets at all 26 stations in this area are used to investigate the spatial variation characteristics of the ionospheric VTEC. Results indicate that the maximum spatial difference at the same moment reaches 51 TECU, 39 TECU, 59 TECU and 30 TECU on the vernal equinox, summer solstice, autumn equinox and winter solstice, respectively. This reveals a significant spatial difference over the Asia-Pacific area. In summary, the BDS GEO satellites provide a new means for ionospheric TEC monitoring. With the forthcoming full deployment of the BDS system, a broader application prospect can be expected.

Acknowledgments

The financial support from the National Key Research and Development Program of China (Grant No. 2016YFB0501803) and the National Natural Science Foundation of China (Grant No. 41674039) are greatly appreciated. The joint teacher-student innovation and entrepreneurship project at Central South University (Grant No. 2018gczd005) is also appreciated. The contribution of data from IGS is appreciated.

ORCID iDs

Changsheng Cai https://orcid.org/0000-0002-5977-4057

References

[1] Ho C M, Mannucci A J, Lindqwister U J, Pi X and Tsurutani B T 1996 Global ionosphere perturbations monitored by the Worldwide GPS Network Geophys *Res. Lett.* **23** 3219–22

[2] Jin S, Park J U, Wang J L, Choi B K and Park P H 2006 Electron density profiles derived from ground-based GPS observations *J. Navig.* **59** 395–401

[3] Sentürk E and Çepni M S 2018 Ionospheric temporal variations over the region of Turkey: a study based on long-time TEC observations *Acta Geod. Geophys.* **53** 623–37

[4] Tu R, Zhang H, Ge M and Huang G 2013 A real-time ionospheric model based on GNSS precise point positioning *Adv. Space Res.* **52** 1125–34
[5] Jarmolowski W, Ren X, Wielgosz P and Krypiak-Gregorczyk A 2019 On the advantage of stochastic methods in the modeling of ionospheric total electron content: Southeast Asia case study *Meas. Sci. Technol.* **30** 044008
[6] Choi K H, Lim J H, Yoo W J and Lee H K 2018 Distributed processing of a GPS receiver network for a regional ionosphere map *Meas. Sci. Technol.* **29** 015104
[7] Liu L, Wan W, Ning B and Zhang M L 2009 Climatology of the mean total electron content derived from GPS global ionospheric maps *J. Geophys. Res-Space Phys.* **114** A6
[8] Wu S, Zhang K, Wu F, Yuan Y and Wu F 2006 Spatio-temporal Characteristics of the Ionospheric TEC Variation for GPSnet-based real-time positioning in Victoria *J. Glob. Position. Syst.* **5** 52–7
[9] Tariku Y A 2015 Patterns of GPS-TEC variation over low-latitude regions (African sector) during the deep solar minimum (2008 to 2009) and solar maximum (2012 to 2013) phases *Earth Planets Space* **67** 35
[10] ŠAuli P, Roux S G, Abry P and BošKa J 2007 Acoustic-gravity waves during solar eclipses: detection and characterization using wavelet transforms *J. Atmos. Sol.-Terr. Phys.* **69** 2465–84
[11] Liu J Y 2009 Seismoionospheric GPS total electron content anomalies observed before the 12 May 2008 Mw7.9 Wenchuan earthquake *J. Geophys. Res-Space Phys.* **114** 231–61
[12] Afraimovich E L, Ding F, Kiryushkin V V, Astafyeva E I, Jin S and Sankov V A 2010 TEC response to the 2008 Wenchuan Earthquake in comparison with other strong earthquakes *Int. J. Remote Sens.* **31** 3601–13
[13] Afraimovich E L *et al* 2013 A review of GPS/GLONASS studies of the ionospheric response to natural and anthropogenic processes and phenomena *J. Space Weather Space Clim.* **3** A27
[14] Sharma S, Galav P, Dashora N and Pandey R 2011 Longitudinal study of the ionospheric response to the geomagnetic storm of 15 May 2005 and manifestation of TADs *Ann. Geophys.* **29** 1063–70
[15] Yang H, Yang X, Zhang Z and Zhao K 2018 High-Precision Ionosphere Monitoring Using Continuous Measurements from BDS GEO Satellites *Sensors* **18** 714
[16] Jin S, Jin R and Kutoglu H 2017 Positive and negative ionospheric responses to the March 2015 geomagnetic storm from BDS observations *J. Geodesy* **91** 613–26
[17] Mannucci A J, Wilson B D, Yuan D N, Ho C H, Lindqwister U J and Runge T F 1998 A global mapping technique for GPS-derived ionospheric total electron content measurements *Radio Sci.* **33** 565–82
[18] Cai C, Liu Z, Xia P and Dai W 2013 Cycle slip detection and repair for undifferenced GPS observations under high ionospheric activity *GPS Solut.* **17** 247–60
[19] Cai C, He C, Santerre R, Pan L and Zhu J 2016 A comparative analysis of measurement noise and multipath for four constellations: GPS, BeiDou, GLONASS and Galileo *Surv. Rev.* **48** 287–95
[20] Montenbruck O, Hauschild A and Steigenberger P 2014 Differential code bias estimation using multi-GNSS observations and global ionosphere maps *Navigation* **61** 191–201
[21] Wang N, Yuan Y, Li Z, Montenbruck O and Tan B 2016 Determination of differential code biases with multi-GNSS observations *J. Geodesy* **90** 209–28
[22] Cai C, Gong Y, Gao Y and Kuang C 2017 An approach to speed up single-frequency PPP convergence with quad-constellation GNSS and GIM *Sensors* **17** 1302
[23] Coster A, Williams J, Weatherwax A, Rideout W and Herne D 2013 Accuracy of GPS total electron content: GPS receiver bias temperature dependence *Radio Sci.* **48** 190–6
[24] Brunini C and Azpilicueta F 2010 GPS slant total electron content accuracy using the single layer model under different geomagnetic regions and ionospheric conditions *J. Geodesy* **84** 293–304
[25] Liu J, Chen R, Wang Z and Zhang H 2011 Spherical cap harmonic model for mapping and predicting regional TEC *GPS Solut.* **15** 109–19
[26] Orús R, Hernández-Pajares M, Juan J M and Sanz J 2005 Improvement of global ionospheric VTEC maps by using Kriging interpolation technique *J. Atmos. Sol.-Terr. Phys.* **67** 1598–609
[27] Nava B, Coisson P and Radicella S M 2008 A new version of the NeQuick ionosphere electron density model *J. Atmos. Sol.-Terr. Phys.* **70** 1856–62
[28] Yu T, Wan W, Liu L and Zhao B 2004 Global scale annual and semi-annual variations of daytime NmF2 in the high solar activity years *J. Atmos. Sol.-Terr. Phys.* **66** 1691–701
[29] Rishbeth H, Sedgemore-Schulthess K J F and Ulich T 2000 Semiannual and annual variations in the height of the ionospheric F2-peak *Ann. Geophys.* **18** 285–99